



Engineering of reduced graphene oxide on nanosheet-g-C₃N₄/perylene imide heterojunction for enhanced photocatalytic redox performance



Liping Yang^{a,b,c}, Pengyuan Wang^b, Jiao Yin^b, Chuanyi Wang^{d,*}, Guohui Dong^{d,*}, Yuanhao Wang^{b,*}, Wingkei Ho^{a,*}

^a Department of Science and Environmental Studies and State Key Laboratory in Marine Pollution, Education University of Hong Kong, Tai Po, New Territories, Hong Kong, China

^b Laboratory of Environmental Science and Technology, Xinjiang Technical Institute of Physics and Chemistry, Key Laboratory of Functional Materials and Devices for Special Environments, Chinese Academy of Sciences, Urumqi 830011, PR China

^c University of Chinese Academy of Sciences, Beijing 100049, PR China

^d School of Environmental Science and Engineering, Shaanxi University of Science and Technology, Xi'an, PR China

ARTICLE INFO

Keywords:

Z-scheme ternary heterojunction
rGO
PTCDI
g-C₃N₄
Photocatalytic NO removal

ABSTRACT

g-C₃N₄-based photocatalysts are recognized as promising candidates for photocatalytic purification of air and solar energy conversions; but their practical application is still limited by the sluggish charge transfer dynamic. Herein, a Z-scheme ternary heterojunction (nanosheet-g-C₃N₄ [NCN]/perylene imide [PI]/reduced graphene oxide [rGO], NCN/PI/rGO) was successfully constructed. For experimental comparison, NCN/rGO/PI was concurrently synthesized through different reaction sequences. In these ternary heterojunction systems, the introduction order of rGO affects the morphology structure and the interaction between phases and results in two diverse electron transfer modes which determine the different photocatalytic redox performances. The as-obtained NCN/PI/rGO Z-scheme heterostructure exhibited superior photocatalytic activity towards the photocatalytic removal of NO and generation of H₂O₂ under visible light irradiation. Such photocatalytic activity was about 1.58 and 1.23 times higher than those of NCN and NCN/PI, respectively, in NO removal. Such enhanced photocatalytic properties can be ascribed to the two-step electron transfer process involving the CB electrons in PI combined with the VB holes of NCN via the Z-scheme pathway (process I, PI→NCN) because PI was grown in situ on the NCN through thermal condensation polymerisation. This process enabled intimate contact between NCN and PI and a short charge-transfer distance. The residual electrons in the CB of NCN then flowed into the rGO (process II, PI→NCN→rGO). Thus, the simultaneous occurrence of two electron transfers processes I and II help improve the photocatalytic activity. Constructing NCN/PI/rGO Z-scheme heterostructures is anticipated to be an effective strategy for developing high-performance photocatalysts that facilitate the utilisation of solar energy.

1. Introduction

Semiconductor-based photocatalysis is a promising strategy for converting solar energy into other energy forms and for abating air pollution [1–5]. For energy conversion, solar energy can be stored in the form of chemical energy, such as, hydrogen peroxide (H₂O₂) has been considered as a tempting solar fuel in place of hydrogen due to its strengths on easy storage and high energy density, which has been used as a single-chamber fuel cell to generate electricity with only oxygen (O₂) and water as by-product, which is a likely clean energy without pollution [6]. Meanwhile, there is a strong demand using solar energy as a primary energy source to purify the air. According to the survey

[7], nitric oxide (NO) and nitrogen dioxide (NO₂) are the main air pollutants produced by the combustion of fuels such as in automobiles and power stations in air. Although most of these emissions are initially in the form of NO, they can be gradually oxidized in the atmosphere to form toxic NO₂, leading to far exceed the NO_x target value of human health. And that, the NO_x are an important cause of acid rain, photochemical smog and sick building syndrome. Due to the prevalence of NO_x, there is great interest in the study of semiconductor photocatalyst for the removal of NO_x.

Recently, metal-free organic polymeric graphitic carbon nitride has been considered as one of the most promising candidates in photocatalysis under visible light mainly owing to relatively narrow band gap

* Corresponding authors.

E-mail addresses: wangchuanyi@sust.edu.cn (C. Wang), donggh@ms.xjb.ac.cn (G. Dong), wangyh@ms.xjb.ac.cn (Y. Wang), keithho@eduhk.hk (W. Ho).

of 2.7 eV, easy preparation, low cost and excellent durability [8,9]. However, the high carrier recombination rate and inadequate absorption of only visible light below 460 nm severely limit the photocatalytic activity of pure bulk g-C₃N₄ [3]. Accordingly, g-C₃N₄-based photocatalysts owning better photo-generated carriers separation and transfer efficiency than its pure bulk counterpart have been explored with many efforts. From this prospect, numerous modification methods, such as doping metal [10–12], controlling morphology [13–15], manufacturing defects [16,17], loading cocatalyst [18,19] and constructing multiphase composite systems, have been explored [20–22]. In particular, constructing a heterogeneous photocatalytic system is an efficient strategy due to the wide range of visible light absorption and efficient carrier spatial separation efficiency.

The gC₃N₄based heterostructures not only inhibits the recombination of photogenerated charge carriers, but also imparts new features to the photocatalysts due to the synergy between gC₃N₄ and other components in the heterostructures. A direct Z-scheme g-C₃N₄/SnS₂ photocatalyst was constructed by Di et al. [23] which has excellent visible light CO₂ reduction performance. The photocatalytic activity of g-C₃N₄/ZnO composites has also reported to be significantly better than that of pure g-C₃N₄ and ZnO for photodegrading of MO and p-nitrophenol under visible light [24]. As another example, Di and co-workers synthesize gC₃N₄/BiOI nanocomposites by a hydrothermal method [25]; the nanocomposites greatly improved the photocatalytic efficiency of gC₃N₄ because of the effective separation of photo-generated electron-hole pairs derived from the matched bandgap structure between gC₃N₄ and BiOI. Although the heterojunction reported above can improve the photocatalytic efficiency, it also has a variety of disadvantages. For example, the oxidation and reduction abilities of the valence-band holes and the conduction-band electrons from a traditional heterojunction are limited; besides, there is a corrosion phenomenon and the photocatalytic stability of g-C₃N₄-based complex is also poor. Thus, in our previous work [26,27], an all-solid Z-scheme heterojunction system was constructed by in situ assembly of PTCDI (PTCDIs, which are perylene imides (PIs), have been proven as a promising photosensitizer due to their strong visible light absorption) via chemical reaction on the surface of gC₃N₄, namely PI-gC₃N₄, with which the photogenerated electrons and holes can be separated into two different phases, helping spatially isolate the oxidation and reduction reaction sites, enhancing the redox capacity and minimizing the catalytic deactivation, leading to the enhancement of photocatalysis efficiency. Despite these advances, binary PI-gC₃N₄ composites are still limited in photocatalytic activity because of the sluggish charge transfer dynamic in the composite system [20,21,28]. To address this issue, a ternary composite system is proposed through incorporating a cocatalyst, which not only can increase the redox reaction sites, but also suppresses the recombination of charge carriers and reduces the activation energy of reaction.

In recent years, combining semiconductor with graphene oxide (GO) or reduced graphene oxide (rGO) have been proven to be an effective method for improving photocatalytic performance [20–22,29–44]. rGO is an electron acceptor and transporter that can enhance the photocatalytic performance of a semiconductor by facilitating the rapid separation and transfer of photogenerated electrons to impede the electron-hole recombination from the semiconductor. Given its superior charge transfer ability, rGO can be used as a cocatalyst to construct a novel solid-state Z-scheme photocatalytic system based on nanosheet-g-C₃N₄ (NCN) and PI. In the present work, rGO was employed to act as an electron acceptor for extracting photogenerated electrons from NCN/PI. More importantly, rGO has a similar sheet structure as that of NCN incorporated with PI in suit and thus can achieve a large and intimate two-dimensional nanojunction. As such, it is expected that rGO will play an important role in determining the carrier separation efficiency and photocatalytic activity.

The purpose of this work was to construct a ternary photocatalyst systems involving NCN modified by PI and rGO. For comparison, two ternary heterojunction systems (NCN/PI/rGO and NCN/rGO/PI) were

synthesized through different reaction sequences. The introduction order of rGO affects the morphology structure and the interaction between phases of the ternary complex and hence results in diverse electron transfer modes which determine the different photocatalytic redox performances. The as-obtained NCN/PI/rGO Z-scheme heterostructure exhibited a superior photocatalytic activity in the photocatalytic removal of NO and generation of H₂O₂ under visible light. The photocatalytic enhancement mechanism of NCN/PI/rGO was also explored, which can be mainly ascribed to the two-step electron transfer process (process I via the Z-scheme pathway, PI→NCN; process II, PI→NCN→rGO). Such simultaneous occurrences of electron transfer processes I and II help improve the photocatalytic activity. This work emphasizes an easy method to further promote the efficiency of carrier separation for heterojunction systems. This approach is proven to be an effective countermeasures for developing high efficiency photocatalysts towards better utilisation of solar energy.

2. Experimental section

2.1. Synthesis of GO and NCN

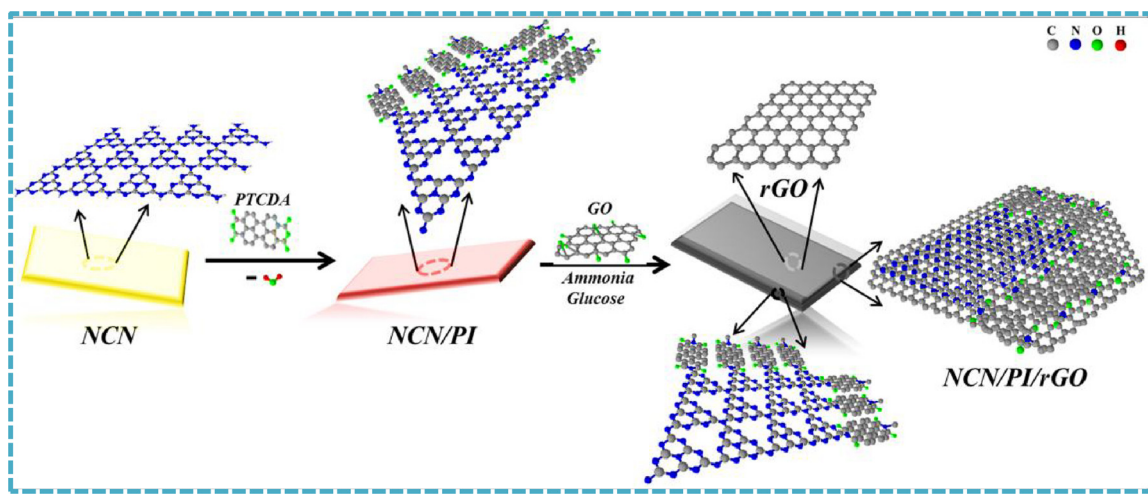
For the synthesis of GO, graphite flakes (3.0 g, 1 wt equiv) were placed in a 500 mL flask, and then 360 mL of concentrated sulfuric acid and 40 mL of concentrated phosphoric acid were slowly added while stirring. After stirring evenly at room temperature, 18 g of potassium permanganate (in three portions, 6 g each time) was added slowly while stirring. Then, the above mixture was stirred 12 h at 50 °C. Subsequently, the mixture in the round-bottom flask was slowly poured onto 400 mL of ice cubes while stirring, after which the temperature was cooled to 50 °C, then adding hydrogen peroxide into it. Finally, the mixture was centrifuged (6000 rpm, 2 h), remaining the precipitate and washed successively with water, HCl (30%) and ethanol. After multiple washes, the material was solidified with 200 mL of ether, and the obtained suspension was filtered through the PTFE membrane. Finally, the remaining solid dried 24 h at 25 °C in vacuo to obtain the sample.

The NCN was prepared using our previous method (seen in Supporting information) [26].

2.2. Synthesis of NCN/rGO and NCN/PI

According to previous reports, the ideal loading amount of GO to g-C₃N₄ was 2.5 wt% [45], which has been confirmed by experiments. Thus, the weight ratio of GO to g-C₃N₄ was also applied in this work. The synthesis of NCN/rGO was accomplished by a high temperature hydrothermal reaction through adding ammonia and glucose [46]. During this process, the oxygen-containing groups of GO tend to conjugate with glucose molecules by electrostatic and hydrogen bonding interactions. This process not only serves as a linker for the NCN, but also can reduce GO to rGO under the action of ammonia. The GO aqueous solution (12.5 mL, 1.4 mg mL⁻¹) was dispersed in NCN aqueous solution (30 mL, 23.3 mg mL⁻¹) while stirring for 30 min by ultrasonic mode. Then, 0.5 g of glucose and 1 mL of ammonia were added while thorough mixing, the mixture was transferred into a 100 mL polyethylene reaction kettle to react 12 h at 180 °C. Until the temperature drops to room temperature, the mixture was filtered and the supernatant discarded. Then, the precipitate was washed several times with ultrapure water and centrifuged until the supernatant was colourless. Finally, the solid obtained in the centrifuge tube was dried at 50 °C for 1 h in vacuum.

Given our previous work, we directly chose the weight percentage of PTCDA to be 5% due to its best performance, and the synthesis process is the same as our previous work (seen in Supporting information) [26].



Scheme 1. Synthetic route of NCN/PI/rGO.

2.3. Synthesis of NCN/rGO/PI and NCN/PI/rGO

To study the effect of the synthetic route on the performance of the final sample, we used two different synthetic sequences. Firstly, rGO was heat reduced to NCN, and then NCN/rGO reacts with PTCDA. The final sample was named NCN/rGO/PI. Secondly, NCN was reacted with PTCDA to generate NCN/PI, and then GO was reduced by hydrothermal process to the NCN/PI surface. The final sample label was NCN/PI/rGO.

For the synthesis of NCN/rGO/PI, the method was the same as the synthesis of NCN/PI. PTCDA was then selected to react with the prepared NCN/rGO via condensation reaction. The weight percentage of PTCDA (0.0355 g) was 5% and the method is the same as that of the synthesis of NCN/PI.

For the synthesis of NCN/PI/rGO (Scheme 1), the method is the same as that of the synthesis of NCN/rGO. The GO aqueous solution (12.5 mL, 1.4 mg mL⁻¹) was dispersed in NCN/PI aqueous solution (30 mL, 23.3 mg mL⁻¹) while stirring for 30 min by ultrasonic energy, and then, 0.5 g of glucose and 1 mL of ammonia were added. After thorough mixing, the mixture was moved to a 100 mL polyethylene reaction kettle to react at 180 °C for 12 h. After cooling to room temperature, the mixture was filtered and the supernatant discarded. Then, the mixture was filtered several times with deionised water until the filtrate was colourless. Finally, the solid obtained on the filter was vacuum dried at 50 °C for 1 h.

3. Result and discussion

3.1. Structural and morphological analyses

Fig. 1a shows the photographs of pure NCN, NCN/rGO, NCN/rGO/PI, NCN/PI and NCN/PI/rGO nanocomposites. Pure NCN is yellow, and rGO and PI introduction induced colour changes change to dark grey for NCN/rGO, pink for NCN/PI, black for NCN/rGO/PI and light grey for NCN/PI/rGO. With the introduction of different amounts of PI and rGO, the black levels of the samples are different, resulting in a difference in colors. A similar phenomenon was also observed in other carbon/semiconductor composites [22,38,43]. Fig. 1b displays the XRD patterns of the prepared samples. There were two diffraction peaks which corresponded to the interlayer stacking ($2\theta = 13.1^\circ$, (100) crystal planes) and interplanar stacking at ($2\theta = 27.3^\circ$, (002) crystal planes) of NCN, respectively. For the NCN/PI, no other diffraction peak was observed, which is most likely because of the weak diffraction intensity or the low content of PI in the complex. However, the change in the (100) peak was stronger than that of NCN when PI is introduced. This result indicates an increase in NCN/PI units in plane. As reported previously, pure GO and rGO have their own characteristic diffraction peaks at 10.8° and 25.1°, respectively [45,47]. However, for NCN/rGO, NCN/rGO/PI and NCN/PI/rGO, no peak was found at 10.8° and a shoulder peak was noted at approximately 25.1°; the latter belonged to the overlapping peaks of rGO and NCN. This finding suggests that most oxygen functional groups of GO were reduced, which benefits for the increasing electrical conductivity. Moreover, after introducing rGO into the NCN/PI, the peak intensity of (002) was increased. This effect can be ascribed to an increased length of the NCN-based nanosheet

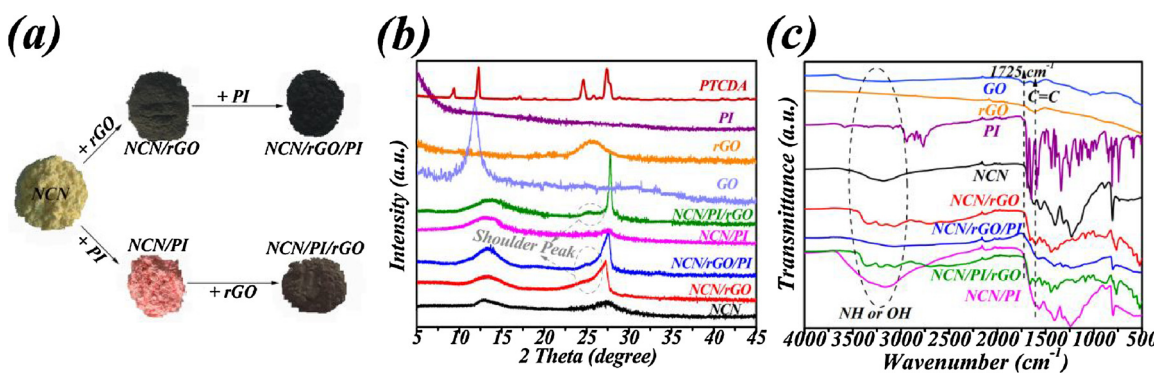


Fig. 1. (a) All solid samples showing different colours; (b) XRD patterns of all samples; (c) FTIR spectra of all samples. (For interpretation of the references to colour in the text, the reader is referred to the web version of this article.)

structure associated with the introduction of large-sized rGO sheets. These results demonstrate the formation of nanocomposites with a layered structure.

To further confirm the existed bonding in NCN/rGO/PI and NCN/rGO, Fourier transform infrared (FTIR) spectroscopic analysis was conducted (Fig. 1c). Pure NCN and NCN/PI presented similar characteristic absorption bands with three main absorption regions at 3200–3600 cm⁻¹ (N–H and O–H bonds), 1800–1200 cm⁻¹ (CN heterocycles in NCN and PI) and below 800 cm⁻¹ (stretching mode of the triazine units), but the peaks for the amide nitrogen functional groups of PI are difficult to identify, because most of these peaks are highly overlapped with those of NCN. Moreover, GO shows absorption peaks belong to the stretching vibration of O=C–OH (1725 cm⁻¹), C–OH (3403 and 1398 cm⁻¹), C=C (1645 cm⁻¹) and C–O (1072 cm⁻¹) [48]. The characteristic peak of O=C–OH (1725 cm⁻¹) did not appear in the spectra of NCN/rGO, NCN/rGO/PI and NCN/PI/rGO, and the intensity of absorption peaks of the oxide groups (OH and C–O) was decreased, suggesting that GO was reduced to rGO.

XPS was further conducted to analyse the surface chemical states of the NCN/PI/rGO and NCN/rGO/PI samples. Three species were detected including carbon, nitrogen and oxygen (Fig. 2a). In the survey spectrum, the peak intensity of oxygen was greatly decreased in NCN/PI/rGO compared with that in NCN/rGO/PI. This effect suggests that the oxygen functional group of GO is further reduced. For the high-resolution C 1s spectrum (Fig. 2b), four distinct peaks appeared centred at 284.6, 285.5, 288.1 and 289.5 eV and correspond to C–C, C–O, N–C=N (in NCN) and C=O (in PI), respectively [49]. By comparison, the peak intensity of NCN/rGO/PI at 289.5 eV was substantially weakened, indicating that changing the introduction sequence of rGO affects the amount of PI assembly on NCN. The N 1s level (Fig. 2c) showed four peaks, which belonged to the N atoms of the melem peripheral (398.5 eV), melem amines (399.5 eV), imides for PI units (400.1 eV) and melem centre (401.1 eV) [49]. Similarly, the peak area of imides for the PI units was remarkably decreased compared with that of NCN/rGO/PI, and the position of this peak was shifted. These results suggest that the amount of PI modified in NCN is decreased while the surrounding chemical environment of the imide groups is also changed. For two composites, there were higher binding energies of the C and N than those of NCN and NCN/PI (Fig. S1). This change in binding energy

and intensity indicates the possibility of electronic interactions between NCN and the other composite components. Obviously, the functional groups in the three-phase composites are mainly derived from the rGO, PI and NCN; this finding implied that the NCN nanosheets are well incorporated with PI and rGO.

Further information on the microstructure and morphology of the prepared samples was obtained by SEM and TEM. As shown in Fig. S2, the SEM images clearly showed the characteristics of the ultrathin nanosheets for NCN, and the other samples all possessed lamellar structures. In addition, high-resolution TEM images (Fig. 2d) of NCN/rGO/PI displayed 2D sheets with corrugation and illustrated that rGO was overlain on the surface of NCN or part of the NCN was wrapped in rGO. However, NCN/PI/rGO showed a flat 2D layer attributed to the rGO with a uniform connection to the NCN/PI surface. This diversity in morphology indicates the different connections between NCN and rGO that will certainly affect the photocatalytic performance. Besides, rGO can be distinguished from NCN/rGO because of the former's peculiar morphology and structure and appeared to be more transparent than NCN in the TEM images [50,51]. Accordingly, an obvious interface between NCN/PI and rGO was observed, indicating their compact lamination, which greatly facilitates rapid interfacial carriers transfer, and then promotes the photocatalytic activity.

3.2. Optical and photoelectrochemical properties

The absorption spectra of all samples were examined by UV-vis DRS. As presented in Fig. 3a, UV-vis DRS analysis reveals that the band gap absorption edge of NCN is about 450 nm. The absorption band of the PTCDA in the visible-light region is known to be approximately 610 nm. Expectedly, modifying PI extends the absorption of NCN in the visible region, which is the characteristic of PI in the solid state. Meanwhile, a small blue shift was detected due to the intermolecular interaction occurring between PI and NCN. With rGO loading, NCN/PI/rGO and NCN/rGO/PI showed an obvious enhancement in absorption over the entire visible wavelength range. This effect is due to that rGO possesses a strong absorption in the visible light region which is advantageous for the high light-capturing efficiency of the rGO-based composite [50].

PL analysis was used to investigate the separation efficiency of the

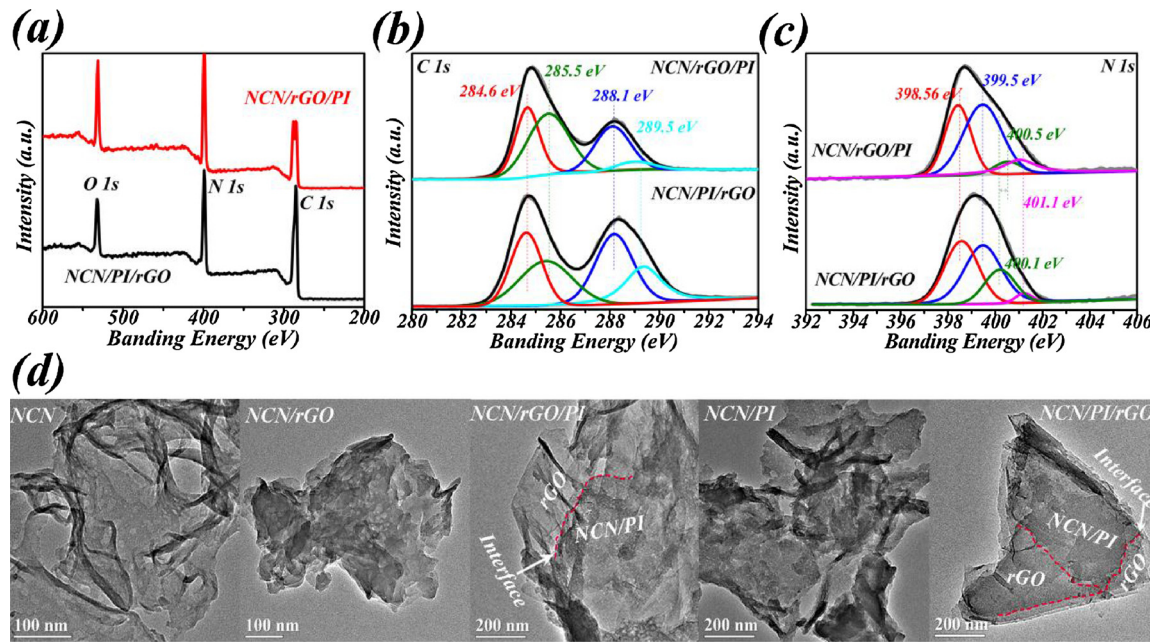


Fig. 2. (a) XPS spectra of NCN/rGO/PI and NCN/PI/rGO; high-resolution XPS spectra of C 1s (b) and N 1s (c) of NCN/rGO/PI and NCN/PI/rGO; (d) TEM images of all samples.

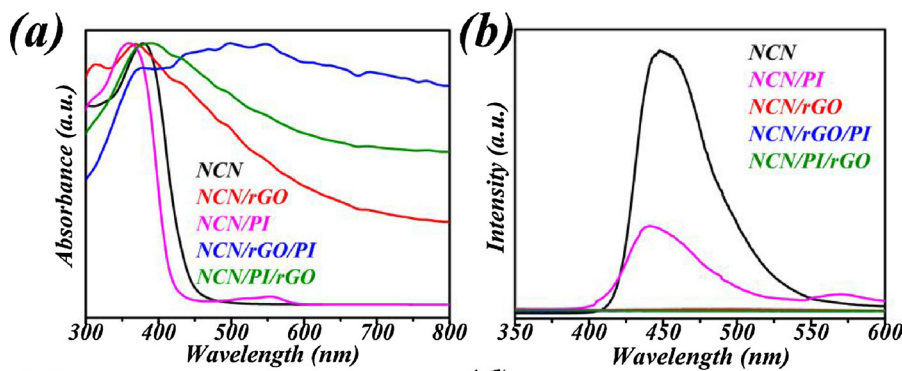


Fig. 3. (a) UV-vis DRS results of all samples; (b) PL spectra of all samples (excited at 315 nm); (c) transient photocurrent responses of all samples under visible-light irradiation; (d) EIS Nyquist plots in the dark in a 0.1 M Na_2SO_4 aqueous solution. (For interpretation of the references to colour in the text, the reader is referred to the web version of this article.)

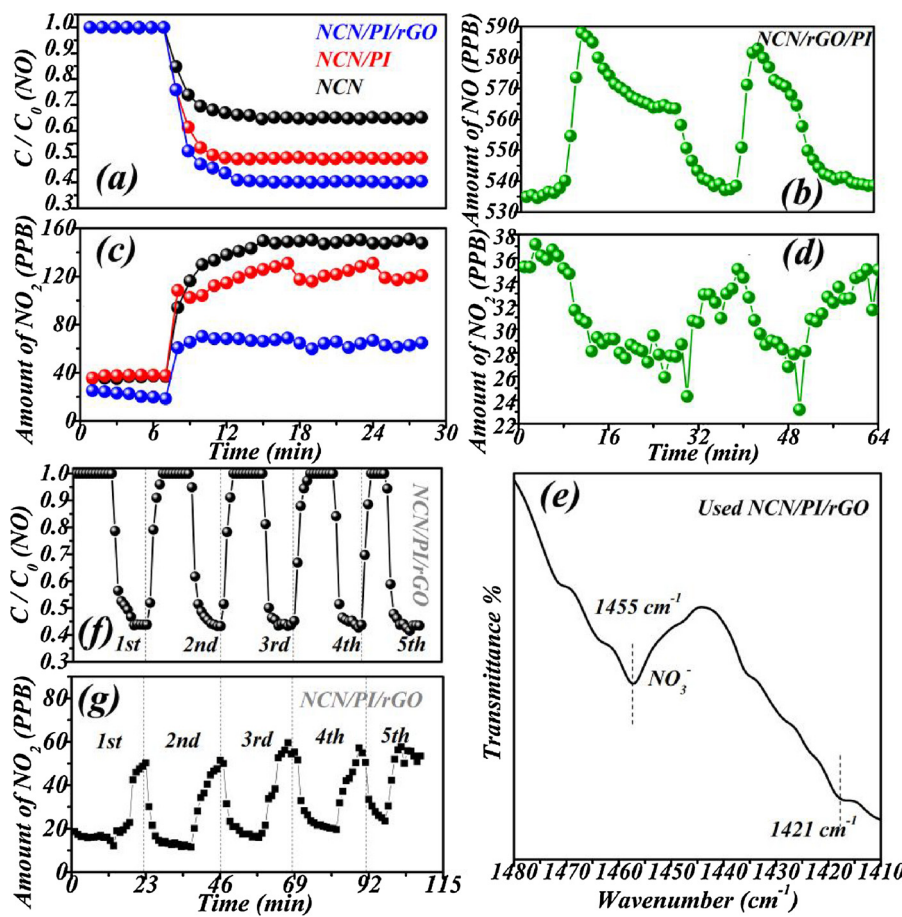
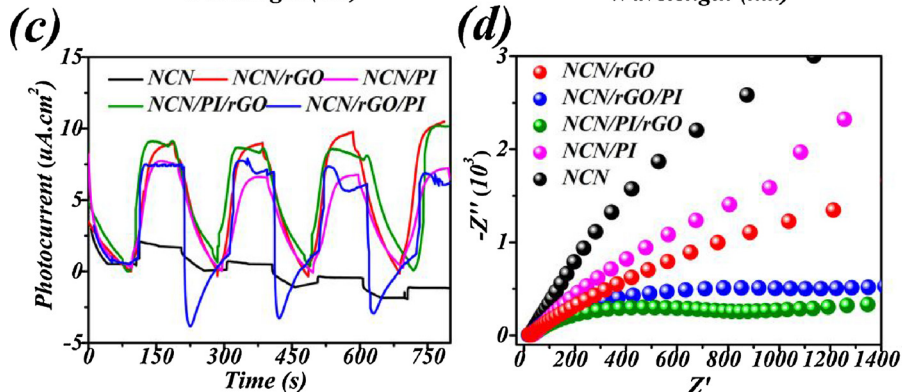


Fig. 4. Relative change in NO concentration (C/C_0) as a function of irradiation time tested over NCN/PI/rGO (a) and NCN/rGO/PI (b) systems, respectively; NO_2 concentration changes with irradiation time tested over NCN/PI/rGO (c) and NCN/rGO/PI (d) systems, respectively; (e) FTIR spectra of NCN/PI/rGO after use in the photocatalytic removal of NO; repeated testing of the photocatalytic NO removal over NCN/PI/rGO (e); NO_2 concentration changes in repeated testing over NCN/PI/rGO (g).

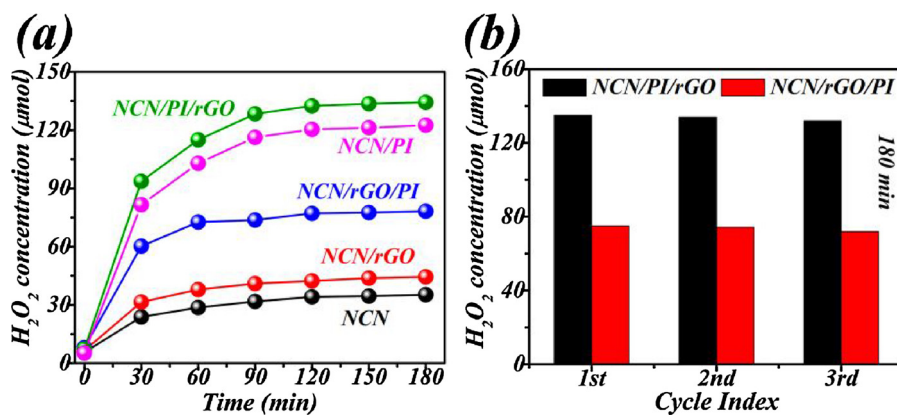


Fig. 5. (a) Concentration of H_2O_2 generated in all samples; (b) Concentration of H_2O_2 generated in NCN/PI/rGO and NCN/rGO/PI systems under 180 min illumination through several circle times.

photogenerated charge carriers in the semiconductors. As shown in Fig. 3b, the emission peak for pure NCN appeared at about 470 nm, and a prominent fluorescence (peak at 571 nm) was observed for NCN/PI indicating the existence of PI. This observation further confirms the surface modification of NCN by PI in compliance with the XPS results above. The emission of NCN/PI blue shifts relative to the spectra of NCN, and this shift is ascribed to the existence of a chemical bonding force between NCN and PI. After instruction of rGO, the position of the emission peak in the PL spectrum was analogous to the NCN, but the intensity was completely quenched, which suggest that the recombination of charge was greatly suppressed by introducing rGO in two ternary complexes. Considering the heterojunction established between NCN and PI, when rGO-based compounds were excited under visible-light irradiation, the excited-state electrons could transport from the conduction band (CB) of NCN/PI to the rGO sheets. Such electron transport help prevent the direct recombination of electrons and holes, thus leading to the improvement in photocatalytic activity.

Electrochemical measurements were performed to further investigate the separation and recombination efficiency of the photo-generated carriers. As shown in Fig. 3c, photocurrent transient responses for NCN were so weak because of the rapid recombination of photogenerated electron-hole pairs. In line with our previous work, the NCN/PI shows a relatively substantial enhancement in photocurrent density over that of NCN. It is supposed that the formation of the heterojunction contributes to the electron transport. Expectedly, the photocurrents of the samples loaded the rGO are much larger than those of NCN/PI and pure NCN, and the intensities are comparable. These results indicate the highest separation efficiency of the carriers. Meanwhile, electrochemical impedance spectroscopy (EIS) was tested to investigate the interfacial charge transfer. Generally, the smaller the semi-arc in the EIS spectrum, the lower the electron transfer resistance value, which indicates a faster interface charge transfer [26]. As shown in Fig. 3d, the arc radius of the samples followed the order of NCN/PI/rGO < NCN/rGO/PI < NCN/rGO < NCN/PI < NCN, suggesting that the lowered resistance and promoted charge separation and transfer efficiency after NCN combining with PI and rGO.

3.3. Photocatalytic activity and stability

The photocatalytic oxidation ability of the three-phase heterojunction system was evaluated evaluated by photocatalytic removal of NO under visible light irradiation. Fig. 4a and b show the changes in NO concentration (C/C_0) or amount as a function of irradiation time for two three-phase heterojunction systems synthesised through different synthesis sequences. Besides, the amount of NO_2 accompanying was also recorded (Fig. 4c and d). As presented in Fig. 4a and c, neither NCN/rGO/PI nor NCN/rGO demonstrated any catalysis for NO

removal. Interestingly, the NO concentration for NCN/rGO/PI gives an increasing trend, whereas the amount of NO_2 shows a downward trend. Conversely, under the same experimental conditions, NCN/PI/rGO showed a 60% NO removal rate within only 10 min irradiation. This result indicates a much improved photocatalytic oxidation efficiency relative to those of NCN (38%) and NCN/PI (49%). Furthermore, using NCN as catalyst, the amount of NO_2 was gradually increased until it became a constant, which clearly indicates that NO_2 is the main product of the photocatalytic NO removal. Interestingly, replacing with NCN/PI and NCN/PI/rGO, the generation of NO_2 was lower than that in NCN, especially NCN/PI/rGO. From this we suspect that most of the NO_2 is further oxidized to NO_3^- , as confirmed by FTIR spectral tests. The used NCN/PI/rGO showed new bands at about 1455 and 1421 cm^{-1} in Fig. 4e appertained to the antisymmetric stretching vibration modes of the NO_3^- group. These bands further imply that NO_3^- is the major product in NCN/PI/rGO. Typically, the production of NO_3^- clogs the active site of catalysts and results in catalyst deactivation. Thus, we demonstrate the stability and recyclability of NCN/PI/rGO through multiple consecutive photocatalytic experiments. The results evince that NCN/PI/rGO still showed effective NO removal efficiency after repeated experiments, and there was no tendency to decrease (Fig. 4f), and the amount of NO_2 remained the least among all samples (Fig. 4g). From the above discussion, compared to the two-phase system (NCN/PI), we can conclude that NCN/PI/rGO not only greatly improved the removal efficiency of NO, but also the production of NO_3^- did not deactivate the catalyst, which greatly reduced secondary pollution.

The above results suggest the presence of a difference in photocatalytic redox capability between the two ternary heterojunction systems. Compared with NCN and NCN/PI, the NCN/PI/rGO system exhibits a highly efficient and stable photocatalytic NO removal process, and the product is greatly converted into a non-toxic NO_3^- . Hence, the hybridisation of NCN/PI with rGO enhances the separation efficiency of the electron-hole pairs and further accelerates the photocatalytic oxidation reaction. However, the NCN/rGO/PI system demonstrates very different results. We hypothesised that NCN/rGO/PI may be a product of the reduction of NO_2 to NO, thus NCN/rGO/PI should have a strong photocatalysis reduction performance. Subsequently, photocatalytic H_2O_2 generation tests were carried out under visible light at a constant temperature (10 °C). Fig. 5a reveals the time-dependent change in the amounts of H_2O_2 formed in 180 min of reaction on respective catalysts. For the NCN/rGO/PI heterojunction, in the same light irradiation time, additional H_2O_2 was produced than those by NCN and NCN/rGO. Meanwhile, the activity is much enhanced by introducing rGO into NCN/PI. NCN/PI/rGO produced the largest H_2O_2 amount, which is more than twice that of NCN/rGO/PI, and possesses good stability in the cyclic test (Fig. 5b). This result indicates a great influence of the synthesis sequences for the ternary heterojunctions on the

photocatalytic oxidation or reduction ability. Simultaneously, the NCN/PI/rGO system notably exhibits higher photocatalytic ability for producing H₂O₂ than that of NCN/rGO/PI. As reported before, a strong interaction between rGO and NCN is highly important [49]. The integrated photocatalytic NO removal and H₂O₂ production, when hybridised with rGO by sequences, unlike those in Scheme 1, it only slightly enhances the photocatalytic reduction reaction. We believe that the rGO embedding positions in the heterojunctions may be distinctive. For the NCN/rGO/PI, the NCN should be semi-encapsulated by rGO slices without destroying the structure of NCN on the basis of the results of XRD spectrum and NO removal tests. Then, NCN/rGO reacts with PI to introduce a finite number of PI groups; however, for the NCN/PI/rGO, the rGO plane should be parallel to the NCN/PI surface, as indicated by the TEM images. These two different connections result in a great difference in interaction force between rGO and NCN/PI and lead to a diverse photocatalytic redox performance.

In the current NCN/PI/rGO system, the mass ratio of NCN, PI, and rGO is also important for the photocatalytic activity of NCN/PI/rGO. Thus, we performed the synthesis experiments of samples with different mass ratios (NCN:PI:rGO) and tested for the NO removal. First, we synthesized NCN/PI_x with different mass percentages (NCN:PI = 100:2.5/100:5.0/100:7.5), then introduced the same mass ratio of rGO (NCN/PI_x:rGO = 100:2.5), the final samples were labeled as NCN/PI_{2.5}/rGO_{2.5}, NCN/PI_{5.0}/rGO_{2.5}, NCN/PI_{7.5}/rGO_{2.5} separately. As shown in Fig. S3 (the inset is the photos of samples), NCN/PI_{5.0}/rGO_{2.5} exhibits the highest NO removal efficiency, which is consistent with our previous work, indicating that the photocatalytic efficiency could be better promoted when the mass ratio of PI was 5.0%, and the NCN/PI described in the manuscript was NCN/PI_{5.0}. On above basis, selecting NCN/PI_{5.0} as the target sample, rGO with different mass ratios (NCN/PI_{5.0}:rGO = 100:1.5/100:2.5/100:3.5) were introduced and the samples were named NCN/PI_{5.0}/rGO_{1.5}, NCN/PI_{5.0}/rGO_{2.5}, NCN/PI_{5.0}/rGO_{3.5} (Fig. S3). As expected, the results show NCN/PI_{5.0}/rGO_{2.5} still has the highest NO removal rate, whereas the introduction of more rGO reduced the catalytic performance, which has a uniform ratio with our above mentioned in experimental section.

3.4. Band structures and charge transfer mechanism

It is well known that the photocatalytic redox ability of a semiconductor depends on the potential of its valence band and conduction band. Accordingly, the derived electronic band gaps from the Tauc plots were 2.92 eV for pure NCN, 2.39 eV for NCN/rGO, 1.95 eV for NCN/rGO/PI, 3.06 eV for NCN/PI and 2.12 eV for NCN/PI/rGO (Fig. 6a). These values indicate that adding rGO decreases the band gap. Furthermore, the bandgap energy values of the NCN and PI parts in the NCN/PI system are calculated to be 2.78 and 2.14 eV, separately (Fig. 6a inset). Besides, we found that the bandgap of the NCN/PI was widened, which coincides with the blue shift of its fluorescence emission peak in Fig. 3b. This effect should be attributed to the quantum confinement effect and the presence of holes through moving the CB and VB edges [52]. Then, the XPS VB spectra were further analysed to explore the band edges of all samples. Seen in Fig. 6b, the VB of the NCN/rGO/PI (+1.80 V) and NCN/PI/rGO (+2.45 V) became more positive than that of NCN (+1.70 V); hence, it is concluded that this result is the VB position of the PI part of the ternary composites. Considering the band gap changes and a positive shift in the VB, the CBs of the NCN and PI parts from the two ternary composites were calculated on the basis of the formula for calculating the band gap ($E_g = VB - CB$). The CB edge potentials of the PI part are derived to be +0.31 V in the NCN/PI/rGO and -0.34 V in the NCN/rGO/PI. Based on these data, the band structure diagram of NCN/PI/rGO and NCN/rGO/PI are schematically described in Fig. 6c. The above discussions show that, in the NCN/rGO/PI and NCN/PI/rGO systems, there are large differences in the electron transport path and the redox reaction on the semiconductor surface. Hence, according to the band level and surface redox

reaction of NCN/rGO/PI and NCN/PI/rGO, their possible charge transfer modes are discussed.

In accordance with the band structure of the two three-phase heterojunction composites, which can be primarily divided into two different cases: the type II heterojunction for NCN/rGO/PI and Z-scheme system for NCN/PI/rGO. In general, given the more negative VB potential of NCN part (+1.70 V vs. SHE) than the formation potential of ·OH radicals (OH[·]/[·]OH, +1.99 V vs. SHE; H₂O/[·]OH, +2.27 V vs. SHE) [26,53], the VB potential of NCN cannot produce ·OH radicals. Likewise, for the NCN/PI/rGO system, since the O₂/[·]O₂[·] potential is more negative than the CB potential of PI (+0.31 V), the electrons in the CB of PI cannot reduce the oxygen molecules to produce ·O₂[·]. To further elucidate the charge transfer mechanism, the presence of ·O₂[·] and ·OH (in a N₂ atmosphere) was detected using the ESR spectra of 5,5-dimethyl-1-pyrrolidine-N-oxide (DMPO) spin-capture adducts. The characteristic peaks of DMPO-·O₂[·] can be found in the NCN/rGO/PI and NCN/PI/rGO systems (Fig. 7a), and the intensity of DMPO-·O₂[·] adducts for NCN/PI/rGO was substantially increased relative to that of NCN/rGO/PI. This result indicates that the ·O₂[·] can be produced in two ternary systems. As expected, prominent DMPO-·OH signals can be observed in the NCN/PI/rGO composites, but no obvious ESR signal of DMPO-·OH adducts is noted in NCN/rGO/PI (Fig. 7b). These results confirm that the holes generated from only the excitation of NCN/PI/rGO can oxidise the surface-adsorbed OH[·] or H₂O to produce ·OH. Based on the aforementioned results, in the NCN/rGO/PI system, considering that the generation of ·O₂[·] and H₂O₂ is higher than that of NCN while suppressing the formation of ·OH, the charge transfer mode with NCN/PI/rGO should be different. Otherwise, for the NCN/PI/rGO system, if the heterojunction-type charge transfer mechanism is adopted, the photogenerated electrons accumulate on the CB of NCN and holes enrich on the VB of PI. This effect promotes the further reduction of oxygen and generation of ·OH radicals and is consistent with the experimental results involved in the NCN/PI/rGO composite. We believe that the Z-scheme electron transfer between NCN and PI occurs on the ternary system of NCN/PI/rGO, which can be explained on the basis of band potentials (Scheme 2). Under visible light illumination, electrons are transferred simultaneously from the VBs to the CBs of the two semiconductors (NCN and PI). Subsequently, the VB holes in PI that have a strong oxidising potential that predominantly oxidises the OH[·] and H₂O relative to the lower oxidising potential of the VB holes in NCN. The CB electrons of PI combine with the VB holes of NCN via the Z-scheme electron transport (process I, PI→NCN) because PI is grown in situ on the NCN through thermal condensation polymerisation. This polymerisation allows the intimate contact between NCN/PI and a short charge-transfer distance. The electrons remaining in the CB of NCN are then transfer to the rGO (process II, PI→NCN→rGO). Therefore, the simultaneous electron transfer processes I and II eventually lead to electron accumulation on the rGO surface. Thus, the photonic efficiency of NO removal and H₂O₂ generation is additionally promoted. Nevertheless, in accordance with the type II heterojunction mechanism, the conductive rGO in the NCN/rGO/PI composite only acts as an electron transport bridge for accelerating the electron transfer from NCN to PI because the NCN is wrapped by rGO similarly to a core–shell structure, and the Fermi energy level of rGO is lower than that of NCN [54]. Meanwhile, by combining the results of the ·OH detection and the decreasing band gap, we can also draw the holes in the VB of PI synchronously migrating to the VB of NCN (Scheme 2). In these two different ternary heterojunction systems, the introduction order of rGO affects the morphology and the interaction between each phase in the ternary complex and hence varies the electron transfer modes. Finally, the position potential energies of the electrons and holes determine the photocatalytic redox performance.

3.5. Photocatalytic redox reaction mechanism

When semiconductor materials are deposited on rGO sheets, it is

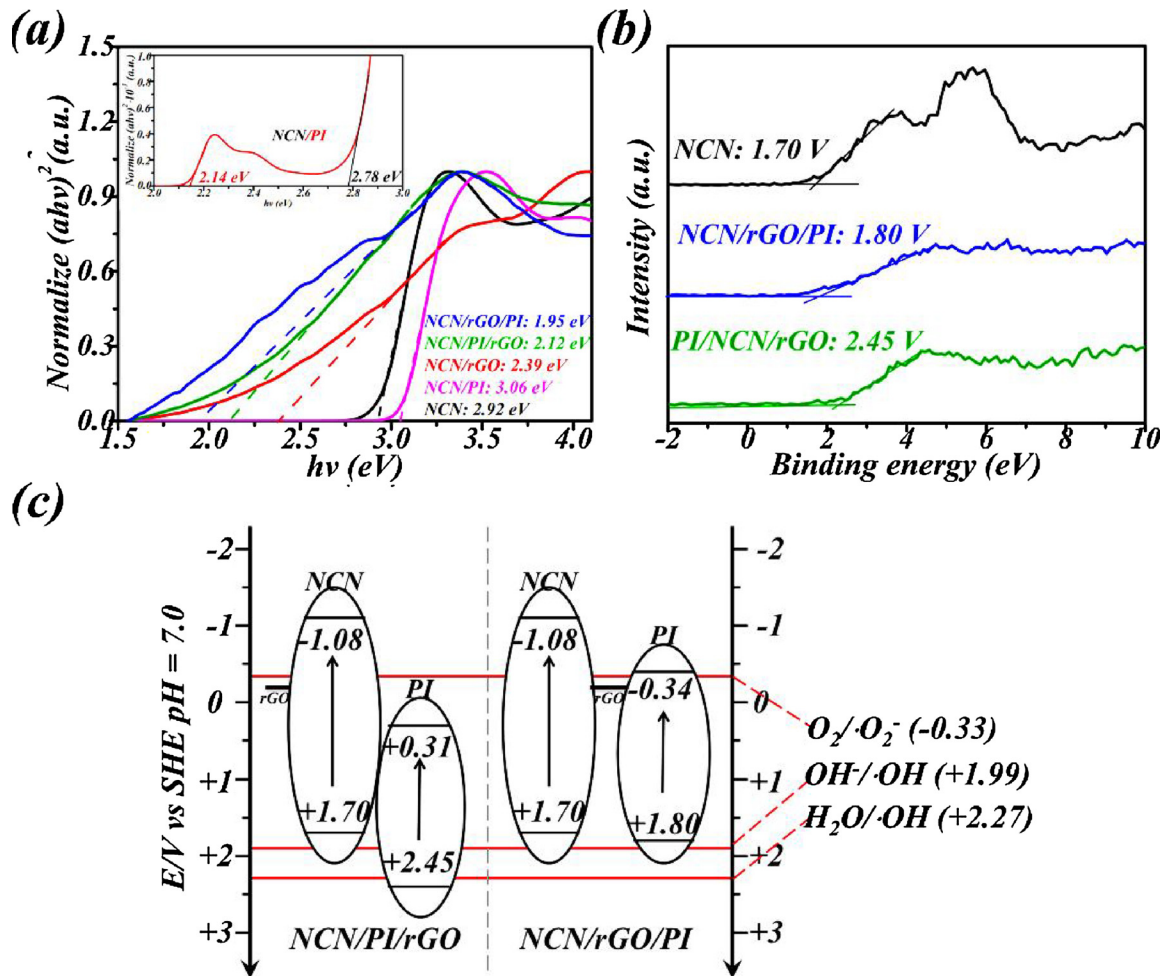


Fig. 6. Band-gap energy of all samples (a) and the NCN and PI parts of NCN/PI (inset); (b) VB XPS of NCN, NCN/PI/rGO and NCN/rGO/PI; and (c) band structures of NCN/PI/rGO and NCN/rGO/PI.

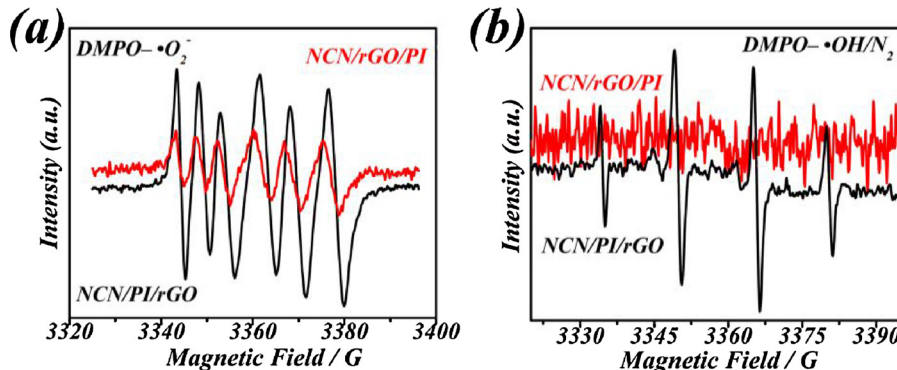
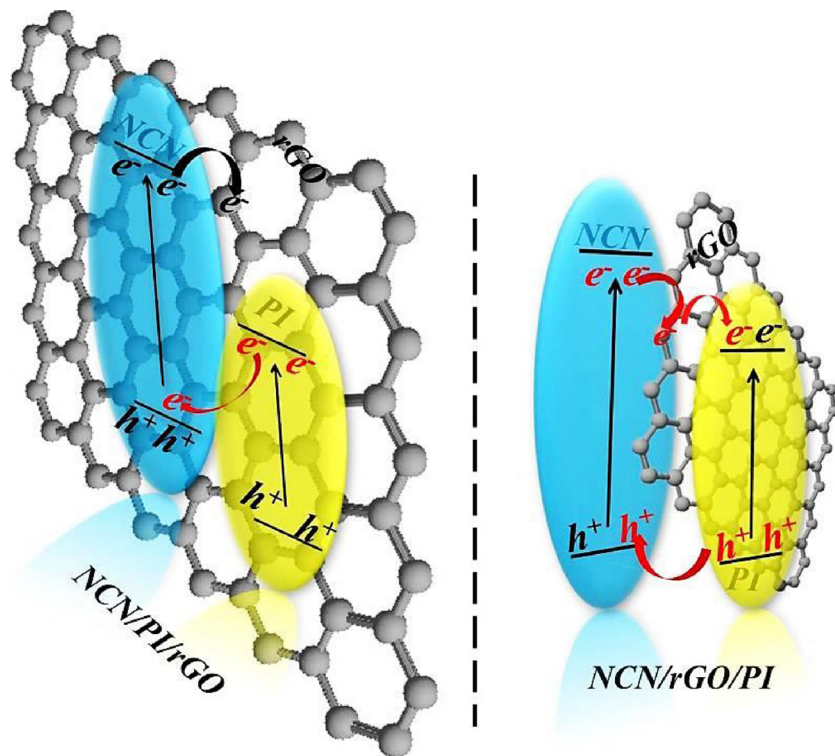


Fig. 7. (a) DMPO spin-trapping ESR spectra recorded for $\cdot O_2^-$ in the NCN/PI/rGO and NCN/rGO/PI systems (under $\lambda > 420$ nm irradiation); (b) DMPO spin-trapping ESR spectra recorded for $\cdot OH$ in the NCN/PI/rGO and NCN/rGO/PI systems under nitrogen conditions (under $\lambda > 420$ nm irradiation).

well known that rGO acts as an electron acceptor by inducing charge carrier separation from a photoexcited semiconductor. Further, efficient charge carrier separation enhances the photocatalytic activity of the rGO-based semiconductor. Therefore, we chose a ternary system of NCN/PI/rGO with good photocatalytic performance to further discuss the photocatalytic mechanism in removing NO.

To determine the dominance of the active species during the photocatalysis process on the NCN/PI/rGO nanocomposite, we used potassium iodide (KI), potassium dichromate ($K_2Cr_2O_7$), tert-butyl alcohol (TBA), p-benzoquinone (PBQ) and catalase (CAT) as scavengers for the quenching of h^+ , e^- , $\cdot OH$, $\cdot O_2^-$ and H_2O_2 , respectively (Fig. 8). In Fig. 8a, when KI was added, the NO removal ability was decreased

obviously, which indicates that holes play the most important role in the photocatalytic removal of NO. However, with the addition of $K_2Cr_2O_7$, TBA, PBQ and CAT, only slight changes are detected in the NO removal ability; this result suggests no substantial contribution from e^- , $\cdot OH$, $\cdot O_2^-$ and H_2O_2 to the photocatalytic removal of NO. In addition, when $K_2Cr_2O_7$ and CAT were added, the amount of NO_2 in the photocatalytic process of NCN/PI/rGO was significantly increased (Fig. 8b). This result indicates that the increasing holes, due to the electrons are trapped, are primarily responsible for oxidising NO to NO_2 , and the elimination of H_2O_2 cannot further oxidize NO_2 to NO_3^- . Based on the above results, we conclude that photogenerated holes and H_2O_2 are essential in the NCN/PI/rGO ternary composite system. The



Scheme 2. Two models of charge separation proposed for NCN/PI/rGO and NCN/rGO/PI systems under visible irradiation. (a) Conventional donor–acceptor charge transfer of NCN/rGO/PI, where the conductive rGO only acts as an electron transport bridge to accelerate the electron transfer from NCN to PI. (b) For NCN/PI/rGO, the simultaneous occurrence of electron transfers I and II in the rGO-promoted Z-scheme heterojunction.

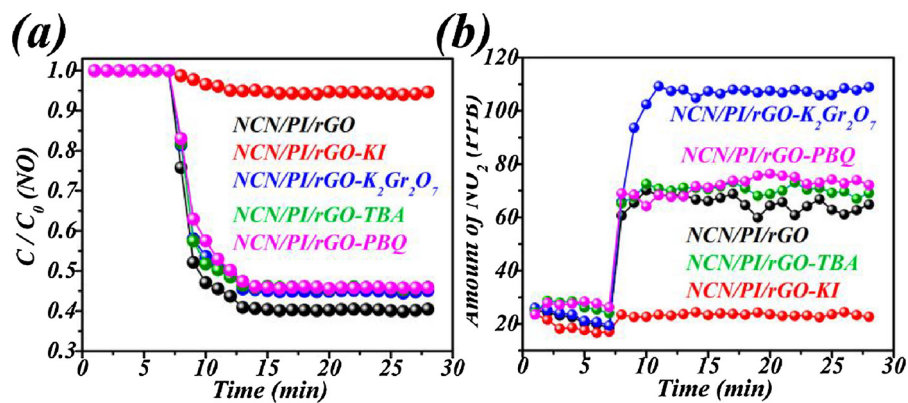
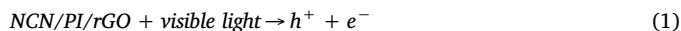


Fig. 8. Influence of different scavengers (KI for h^+ , $\text{K}_2\text{Cr}_2\text{O}_7$ for e^- , TBA for $\cdot\text{OH}$, PBQ for $\cdot\text{O}_2^-$, CAT for H_2O_2) on the photocatalytic removal of NO by using NCN/PI/rGO. The photcatalysis conditions are the same as those in Fig. 4.

above-mentioned components play synergistic roles in NO removal and enables the ultimate conversion from NO_2 to NO_3^- ion (consistent with our previous observation on $\text{PI}-g-\text{C}_3\text{N}_4$). Combined with the EPR results, we conclude that the mechanism of the photocatalytic removal of NO in NCN/PI/rGO proceeds as Eqs. (1)–(7):



During the whole photocatalysis process of NCN/PI/rGO, the photogenerated electrons are mostly transferred to rGO. Consequently, we can obtain that the enhanced photocatalytic performance of NCN/PI/rGO

can be mainly attributed to incorporation of rGO into a Z-scheme heterojunction such as NCN/PI, which transports electrons more efficiently and further promotes the separation of carriers.

4. Conclusion

An all-solid-state Z-Scheme ternary heterojunction (NCN/PI/rGO) was successfully constructed. For experimental comparison, NCN/rGO/PI variations were concurrently synthesized through different reaction sequences. In these two ternary heterojunction systems, the introduction order of rGO affects the morphology and the interaction between phases in ternary complexes and results in diverse electron transfer modes. Finally, the position potential energies of the electrons and holes determine the varying photocatalytic redox performance. The NCN/PI/rGO ternary heterostructure exhibits superior photocatalytic activity for the photocatalytic removal of NO and generation of H_2O_2 under visible-light irradiation. As such, the NCN/PI/rGO ternary heterostructure creates further charge separation with the electrons remaining in the CB of NCN; these electrons thereafter flow into the rGO

(electron transfer, PI \rightarrow NCN \rightarrow rGO) in the rGO-promoted Z-scheme heterojunction, thereby enhancing the redox reaction power of the charge carriers. In addition, the NCN/PI/rGO heterojunction shows good stability in the photocatalytic process of removing NO and generating H₂O₂ and is hence improved in potential commercial value. This study provides new insights into the design of effective photocatalysts that can be operated under visible light and facilitate the utilization of solar energy.

Acknowledgments

This work was supported by the National Key Research and Development Programme of China (2016YFA0203000), the General Research Fund-Research Grant Council of Hong Kong Government (Project No 18301117), Dean's Reserved Fund (04257) and (04317), FLASS, The Education University of Hong Kong. This work was also supported by the National Nature Science Foundation of China (Grant No. Y711611601), the Chinese Government "Thousand Talent" Program (Y62HB31601), the Shenzhen Peacock Plan (KQTD2015071616442225) and the National Nature Science Foundation of China (Grant No. 21876104).

Appendix A. Supplementary data

Supplementary material related to this article can be found, in the online version, at doi:<https://doi.org/10.1016/j.apcatb.2019.02.076>.

References

- [1] J. Fu, J. Yu, C. Jiang, B. Cheng, *Adv. Energy Mater.* 8 (2018) 1701503.
- [2] D. Masih, Y. Ma, S. Rohani, *Appl. Catal. B: Environ.* 206 (2017) 556–588.
- [3] W.J. Ong, L.L. Tan, Y.H. Ng, S.T. Yong, S.P. Chai, *Chem. Rev.* 116 (2016) 7159–7329.
- [4] S. Cao, J. Low, J. Yu, M. Jaroniec, *Adv. Mater.* 27 (2015) 2150–2176.
- [5] X. Wang, S. Blechert, M. Antonietti, *ACS Catal.* 2 (2012) 1596–1606.
- [6] K. Mase, M. Yoneda, Y. Yamada, S. Fukuzumi, *Nat. Commun.* 7 (2016) 11470.
- [7] A. Mills, S. Elouali, *J. Photochem. Photobiol. A* 305 (2015) 29–36.
- [8] Y. Zheng, L. Lin, B. Wang, X. Wang, *Angew. Chem. Int. Ed.* 54 (2015) 12868–12884.
- [9] X. Wang, K. Maeda, A. Thomas, K. Takanabe, G. Xin, J.M. Carlsson, K. Domen, M. Antonietti, *Nat. Mater.* 8 (2008) 76–80.
- [10] C. Sun, H. Zhang, H. Liu, X. Zheng, W. Zou, L. Dong, L. Qi, *Appl. Catal. B: Environ.* 235 (2018) 66–74.
- [11] Y. Zheng, Y. Jiao, Y. Zhu, Q. Cai, A. Vasileff, L.H. Li, Y. Han, Y. Chen, S.-Z. Qiao, *J. Am. Chem. Soc.* 139 (2017) 3336–3339.
- [12] Y. Bu, Z. Chen, W. Li, *Appl. Catal. B: Environ.* 144 (2014) 622–630.
- [13] Z. You, Y. Su, Y. Yu, H. Wang, T. Qin, F. Zhang, Q. Shen, H. Yang, *Appl. Catal. B: Environ.* 213 (2017) 127–135.
- [14] J. Xu, Z. Wang, Y. Zhu, *ACS Appl. Mater. Interfaces* 9 (2017) 27727–27735.
- [15] J. Wang, J. Cong, H. Xu, J. Wang, H. Liu, M. Liang, J. Gao, Q. Ni, J. Yao, *ACS Sustain. Chem. Eng.* 5 (2017) 10633–10639.
- [16] G. Ge, X. Guo, C. Song, Z. Zhao, *ACS Appl. Mater. Interfaces* 10 (2018) 18746–18753.
- [17] G. Dong, D.L. Jacobs, L. Zang, C. Wang, *Appl. Catal. B: Environ.* 218 (2017) 515–524.
- [18] N. Zhao, L. Kong, Y. Dong, G. Wang, X. Wu, P. Jiang, *ACS Appl. Mater. Interfaces* 10 (2018) 9522–9531.
- [19] M. Liu, P. Xia, L. Zhang, B. Cheng, J. Yu, *ACS Sustain. Chem. Eng.* 6 (2018) 10472–10480.
- [20] D. Xu, B. Cheng, W. Wang, C. Jiang, J. Yu, *Appl. Catal. B: Environ.* 231 (2018) 368–380.
- [21] P. Xiao, D. Jiang, L. Ju, J. Jing, M. Chen, *Appl. Surf. Sci.* 433 (2018) 388–397.
- [22] G. Wang, Z. Wen, Y.-E. Yang, J. Yin, W. Kong, S. Li, J. Sun, S. Ji, *J. Mater. Chem. A* 6 (2018) 7557–7565.
- [23] T. Di, B. Zhu, B. Cheng, J. Yu, J. Xu, *J. Catal.* 352 (2017) 532–541.
- [24] J.X. Sun, Y.P. Yuan, L.G. Qiu, X. Jiang, A.J. Xie, Y.H. Shen, J.F. Zhu, *Dalton Trans.* 41 (2012) 6756–6763.
- [25] J. Di, J. Xia, S. Yin, H. Xu, L. Xu, Y. Xu, M. He, H. Li, *J. Mater. Chem. A* 2 (2014) 5340.
- [26] L. Yang, G. Dong, D.L. Jacobs, Y. Wang, L. Zang, C. Wang, *J. Catal.* 352 (2017) 274–281.
- [27] G. Dong, L. Yang, F. Wang, L. Zang, C. Wang, *ACS Catal.* (2016) 6511–6519.
- [28] J. Li, H. Yuan, Z. Zhu, *Appl. Surf. Sci.* 385 (2016) 34–41.
- [29] Y.-J. Yuan, Y. Yang, Z. Li, D. Chen, S. Wu, G. Fang, W. Bai, M. Ding, L.-X. Yang, D.-P. Cao, Z.-T. Yu, Z.-G. Zou, *ACS Appl. Energy Mater.* 1 (2018) 1400–1407.
- [30] Y. Wu, P. Wang, X. Zhu, Q. Zhang, Z. Wang, Y. Liu, G. Zou, Y. Dai, M.H. Whangbo, B. Huang, *Adv. Mater.* 30 (2018) 1704342.
- [31] N. Thangavel, S. Bellamkonda, A.D. Arulraj, R.R. Gangavarapu, B. Neppolian, *Catal. Sci. Technol.* 8 (19) (2018) 5081–5090.
- [32] C. Song, M. Fan, W. Shi, W. Wang, *Environ. Sci. Pollut. Res. Int.* 25 (2018) 14486–14498.
- [33] W. Qian, X. Hu, W. He, R. Zhan, M. Liu, D. Zhou, Y. Huang, X. Hu, Z. Wang, G. Fei, J. Wu, M. Xing, H. Xia, G. Luo, *Colloids Surf. B: Biointerfaces* 166 (2018) 61–71.
- [34] V. Iliev, D. Tomova, L. Bilyarska, *J. Photochem. Photobiol. A* 351 (2018) 69–77.
- [35] J. Hu, D. Chen, N. Li, Q. Xu, H. Li, J. He, J. Lu, *Small* 14 (2018) 1800416.
- [36] B. Gomez-Ruiz, P. Ribao, N. Dibán, M.J. Rivero, I. Ortiz, A. Urtiaga, J. Hazard. Mater. 344 (2018) 950–957.
- [37] Y.F. Xu, M.Z. Yang, B.X. Chen, X.D. Wang, H.Y. Chen, D.B. Kuang, C.Y. Su, *J. Am. Chem. Soc.* 139 (2017) 5660–5663.
- [38] L. Tang, C.-t. Jia, Y.-c. Xue, L. Li, A.-q. Wang, G. Xu, N. Liu, M.-h. Wu, *Appl. Catal. B: Environ.* 219 (2017) 241–248.
- [39] L. Sun, T. Du, C. Hu, J. Chen, J. Lu, Z. Lu, H. Han, *ACS Sustain. Chem. Eng.* 5 (2017) 8693–8701.
- [40] M. Sohail, H. Xue, Q. Jiao, H. Li, K. Khan, S. Wang, Y. Zhao, *Mater. Res. Bull.* 90 (2017) 125–130.
- [41] W.-K. Jo, N.C.S. Selvam, *Chem. Eng. J.* 317 (2017) 913–924.
- [42] D. Jiang, P. Xiao, L. Shao, D. Li, M. Chen, *Ind. Eng. Chem. Res.* 56 (2017) 8823–8832.
- [43] H. Huang, J. Zhang, L. Jiang, Z. Zang, *J. Alloys Compd.* 718 (2017) 112–115.
- [44] S. Song, B. Cheng, N. Wu, A. Meng, S. Cao, J. Yu, *Appl. Catal. B: Environ.* 181 (2016) 71–78.
- [45] Y. Li, H. Zhang, P. Liu, D. Wang, Y. Li, H. Zhao, *Small* 9 (2013) 3336–3344.
- [46] L. Li, J. Qin, H. Bi, S. Gai, F. He, P. Gao, Y. Dai, X. Zhang, D. Yang, P. Yang, *Sci. Rep.* 7 (2017) 43413.
- [47] G. Liao, S. Chen, X. Quan, H. Yu, H. Zhao, *J. Mater. Chem.* 22 (2012) 2721–2726.
- [48] J. Zhang, H. Yang, G. Shen, P. Cheng, J. Zhang, S. Guo, *Chem. Commun.* 46 (2010) 1112–1114.
- [49] Y. Kofuji, Y. Isobe, Y. Shiraishi, H. Sakamoto, S. Tanaka, S. Ichikawa, T. Hirai, *J. Am. Chem. Soc.* 138 (2016) 10019–10025.
- [50] T.-F. Yeh, J.-M. Syu, C. Cheng, T.-H. Chang, H. Teng, *Adv. Funct. Mater.* 20 (2010) 2255–2262.
- [51] S.V. Tkachev, E.Y. Buslaeva, A.V. Naumkin, S.L. Kotova, I.V. Laure, S.P. Gubin, *Inorg. Mater.* 48 (2012) 796–802.
- [52] Q. Han, B. Wang, J. Gao, Z. Cheng, Y. Zhao, Z. Zhang, L. Qu, *ACS Nano* 10 (2016) 2745–2751.
- [53] X. Zeng, Z. Wang, G. Wang, T.R. Gengenbach, D.T. McCarthy, A. Deletic, J. Yu, X. Zhang, *Appl. Catal. B: Environ.* 218 (2017) 163–173.
- [54] A. Benayad, H.-J. Shin, H.K. Park, S.-M. Yoon, K.K. Kim, M.H. Jin, H.-K. Jeong, J.C. Lee, J.-Y. Choi, Y.H. Lee, *Chem. Phys. Lett.* 475 (2009) 91–95.